Neutron diffraction and ultrasonic studies of spin-slip structures in holmium

1997 J. Phys.: Condens. Matter 9 5167

(http://iopscience.iop.org/0953-8984/9/24/015)

J. Phys.: Condens. Matter **9** (1997) 5167–5191. Printed in the UK PII: S0953-8984(97)78781-2

Neutron diffraction and ultrasonic studies of spin-slip structures in holmium*

Andrew M Venter† and Paul de V du Plessis‡

† Atomic Energy Corporation of S A (Ltd), P O Box 582, Pretoria, South Africa

‡ Physics Department, University of the Witwatersrand, Private Bag 3, PO Wits 2050, Johannesburg, South Africa

Received 18 October 1996, in final form 25 March 1997

Abstract. Spin-slip behaviour in high-purity holmium single crystals is characterized by neutron diffraction and ultrasonic velocity and attenuation measurements as a function of temperature and of magnetic field applied along *b*, *c*, and *a* axes. Neutron diffraction measurements of intensity and turn angle give information on wave vector lock-in effects for various spin-slip structures in applied fields. These findings are supplemented with ultrasonic studies of the elastic constants C_{33} and C_{44} and corresponding attenuation coefficients α_{33} and α_{44}. Various phase diagrams are presented and results compared with experiments by other groups and with some theoretical predictions.

1. Introduction

The hexagonal close-packed element holmium orders in a helical magnetic structure below its Néel temperature $T_N \sim 132$ K. In the original model for the spin structure based on the pioneering neutron diffraction studies by Koehler *et al* [1] and subsequent refinements by Felcher *et al* [2] and Pechan and Stassis [3], the spins form ferromagnetic sheets aligned within the basal plane, but with the direction of spins rotated from plane to plane by a turn angle ω. The magnitudes of ω and of the corresponding wave vector $\boldsymbol{\tau}$ were observed to decrease continuously with decreasing temperature from $\boldsymbol{\tau} \sim 0.28\ \boldsymbol{c}^*(c^* = 2\pi/c)$ at T_N to a lock-in transition with a commensurate wave vector $\boldsymbol{\tau} = \frac{1}{6}\ \boldsymbol{c}^*$ at the Curie temperature $T_C \sim 18$ K. The spin structure below T_C is that of a ferromagnetic cone in which the moments are tilted away from the basal plane by approximately 10° (as observed at 4 K). The sixfold anisotropy within the basal plane increases rapidly upon cooling and this leads to fifth and seventh harmonics of τ below 50 K [1]. Pechan and Stassis furthermore suggested the possibility of a modulated *c* axis moment in the helical region of Ho. Koehler *et al* [4] also investigated the spin structure of Ho as a function of magnetic field applied in the basal plane. Complicated magnetic phase diagrams are obtained with the helical structure transformed through intermediate fan structures to an induced ferromagnetic structure at low temperatures. In the vicinity of 40–50 K Koehler *et al* observed a field-induced phase which later turned out to be the helifan (3/2) phase [5–7]. This phase is constructed from portions of the helix and the fan following each other in a periodic way [5].

Using high-resolution x-ray scattering Gibbs *et al* [8] observed in zero field that two other commensurate structures, with $\boldsymbol{\tau} = \frac{2}{11}\ \boldsymbol{c}^*$ and $\boldsymbol{\tau} = \frac{5}{27}\ \boldsymbol{c}^*$, exist in a small temperature

* Dedicated to Professor Richard Lemmer on the occasion of his 65th birthday.

0953-8984/97/245167+25$19.50

interval above T_C. Bohr *et al* [9] interpreted these results in terms of a model based on spin slips or spin discommensurations. In the simplest model, pairs of ferromagnetic planes have their moments aligned along a particular easy magnetization direction in the basal plane (for Ho this is one of the *b* axes), thus giving a region of commensurate spin structure formed by a spiral of doublets. Commensurate regions are separated by a spin slip for which only one plane has its moments along a particular easy direction. When such spin slips are repeated at regular intervals along the *c* axis this results in a particular higher-order commensurate phase.

Cowley and Bates [10] and Bates *et al* [11] performed high-resolution elastic neutron scattering measurements in order to resolve the complicated diffraction patterns associated with the low-temperature spin-slip structure of Ho. In their more refined description the directions of the moments deviate from the easy directions by an angle $\pm\alpha$, $\alpha \approx 10^\circ$, within the commensurate regions. The plane at the spin-slip position retains its moments along the easy direction. Furthermore a Gaussian Debye–Waller factor was used to allow for a change of α for spins closest to a spin slip, as well as for uncertainty in the position of the spin slips due to thermal fluctuations or impurities. Good agreement was obtained between their diffraction results and model calculations. These yield *inter alia* values for the mean spin-slip separation *b*, which increases smoothly from a value of $\sim$2 near 100 K to $\sim$12.5 at 19 K. They observed no preferred *b* values, thus implying free spin-slip movement during thermal cycling of their crystal. This result is in contrast to the synchrotron x-ray results where lock into $\boldsymbol{\tau} = \frac{2}{11}\,\boldsymbol{c}^*$ and $\boldsymbol{\tau} = \frac{5}{27}\,\boldsymbol{c}^*$ structures was observed close to T_C in zero-field measurements [8, 9]. The variation of the superlattice peaks and higher-order satellites in the reciprocal lattice has been followed as a function of temperature. It is observed that for certain temperatures the diffraction peaks cross one another in reciprocal space. These temperatures correspond to supercommensurate structures with values of $b = 2$, 5, 8, and 11. In table 1 a compilation of these supercommensurate structures, as well as the $\boldsymbol{\tau} = \frac{5}{27}\,\boldsymbol{c}^*$, $\boldsymbol{\tau} = \frac{4}{21}\,\boldsymbol{c}^*$, and $\boldsymbol{\tau} = \frac{2}{9}\,\boldsymbol{c}^*$ structures, are given. In the spin-slip model as formulated by Cowley and Bates [10] only odd-integer-*b*-value structures can be uniquely defined. The even-integer-*b*-value structures ($b = 2$ and 8) are constructed by having successive spin slips separated by $b + 1$ and $b - 1$ planes. Spin-slip structures are described in table 1 by writing a '2' to indicate the two planes of a doublet and a '1' to denote the single plane at the spin-slip position. Bates *et al* [11] studied the elastic constants C_{ij} of Ho and observed anomalies in some of these corresponding to the temperatures of the supercommensurate structures (see table 1).

Tindall and collaborators observed in a series of neutron diffraction experiments at Chalk River lock-in behaviour in an applied field whereby $\boldsymbol{\tau}$ takes on a constant unique value over a finite temperature interval. These studies were performed by monitoring the position of the fundamental magnetic diffraction peak as a function of temperature. For *c*-axis-directed fields lock-ins were observed at $\boldsymbol{\tau} = \frac{1}{4}\,\boldsymbol{c}^*$ in 2.2 T [12] and 3 T [13] and at $\boldsymbol{\tau} = \frac{1}{5}\,\boldsymbol{c}^*$ in 3 T [13]. For fields directed along the *b* axis lock-ins were observed at $\boldsymbol{\tau} = \frac{1}{4}\,\boldsymbol{c}^*$ in 3 T [13], at $\boldsymbol{\tau} = \frac{5}{18}\,\boldsymbol{c}^*$ in 3 T between 126 K and $T_N \approx 132.9$ K [13, 14] and at $\boldsymbol{\tau} = \frac{2}{9}\,\boldsymbol{c}^*$ at 75 K in a field of 1.4 T [15]. No lock-in was observed for $\boldsymbol{\tau} = \frac{5}{18}\,\boldsymbol{c}^*$ with a *c*-axis-directed field of 3 T [12]. A two-phase region was indicated in which the $\boldsymbol{\tau} = \frac{5}{18}\,\boldsymbol{c}^*$ phase coexists with an incommensurate phase between 119 and 126 K [14]. In a recent study we reported that the elastic constant C_{33} and attenuation coefficient α_{33} of Ho exhibit marked anomalies [16], which correlate with the temperature extent of the lock-in at $\boldsymbol{\tau} = \frac{5}{18}\,\boldsymbol{c}^*$ as observed with neutron diffraction.

At low temperatures Pearce *et al* [17] observed lock-in for $\boldsymbol{\tau} = \frac{2}{11}\,\boldsymbol{c}^*$ in a small field of 0.03 T directed along the *b* axis. The effect of applying a magnetic field directed along

Table 1. A summary pertaining to supercommensurate (SC) spin-slip structures (as indicated by Bates *et al* [11]), as well as some other spin-slip structures observed for Ho, values of wave vector $\boldsymbol{\tau}$, spin-slip distance b, temperatures where these structures appear and an indication of whether anomalies have been observed (✓) or not (×) in the C_{33}, C_{44}, and C_{11} elastic constants by Bates *et al*. Details relating to the Néel (T_N) and Curie (T_C) temperatures are also included.

T (K)	$\boldsymbol{\tau}$ ($\boldsymbol{c}^*$)	Spin-slip structure	b	C_{33}	C_{44}	C_{11}
17.8 (T_C)	$\frac{1}{6}$	Ferromagnetic cone	—	✓	✓	✓
19.8	$\frac{2}{11}$	222221 (SC)	11	✓	✓	✓
	$\frac{5}{27}$	22221	9			
24.5	$\frac{3}{16}$	222122221 (SC)	8		✓	✓
	$\frac{4}{21}$	2221	7			
75	$\frac{2}{9}$	21	3			
40.5	$\frac{1}{5}$	221 (SC)	5	×	×	×
97.4	$\frac{1}{4}$	211 (SC)	2	×	✓	×
133.4 (T_C)			—	✓	✓	✓

the c axis at low temperatures was investigated by Cowley and coworkers [7, 18]. It was observed that below ≈15 K the field induced spin-slip structures with $\boldsymbol{\tau} = \frac{1}{6}\,\boldsymbol{c}^*$, $\frac{2}{11}\,\boldsymbol{c}^*$, $\frac{3}{16}\,\boldsymbol{c}^*$, $\frac{4}{21}\,\boldsymbol{c}^*$, and $\frac{5}{26}\,\boldsymbol{c}^*$ as it was increased up to 5 T. These wave vectors hence form a devil's staircase [18] with increased applied field. In a magnetic field of up to 0.5 T applied along the easy basal plane b axis, phases with $\boldsymbol{\tau} = \frac{1}{6}\,\boldsymbol{c}^*$, $\frac{2}{11}\,\boldsymbol{c}^*$, $\frac{3}{16}\,\boldsymbol{c}^*$, and $\frac{5}{26}\,\boldsymbol{c}^*$ were obtained [7].

Theoretical work pertaining to the spin-slip concept in Ho includes numerical model calculations by Mackintosh and Jensen [19] of the modifications of the ideal spin-slip structure as well as extensive descriptions and theoretical exposition of the many new developments in rare-earth magnetism during the 1980s [20]. The $\boldsymbol{\tau} = \frac{1}{4}\,\boldsymbol{c}^*$ lock-in at 98 K in Ho has been studied by Plumer [21] in a molecular-field theory which includes magnetoelastic coupling through the variation of Heisenberg exchange interactions with inter-ionic distance. A large symmetry-breaking term in the free energy is assumed in order to distort the polarization of the spin density from helical to elliptical. A magnetic field applied in the basal plane (or a field component within the basal plane) was proposed by Plumer to effect the symmetry breaking, while it was indicated that a field directed exactly along the c axis would have no effect. Jensen [22] argues against the *ad hoc* introduction of a symmetry-breaking term by Plumer, but rather includes a trigonal coupling as has recently been observed by Simpson *et al* [23] in Ho after its initial discovery in Er [24, 25]. Finally, Steinitz *et al* [26] indicated that the commensurate τ values at which lock-in takes place in an applied field for Ho are predictable on the basis of limitations which finite specimen or domain size impose on the possible wave-vector steps which otherwise would form a quasi-continuous devil's staircase in an infinite sample.

In the present study we report on neutron diffraction studies in Ho of lock-in effects at $\boldsymbol{\tau} = \frac{1}{6}\,\boldsymbol{c}^*$ and $\boldsymbol{\tau} = \frac{2}{11}\,\boldsymbol{c}^*$ in b-axis-directed fields at low temperatures, as well as results observed for c-axis-directed fields, and compare our findings with those of other authors [17, 18]. We also report on and extend our phase diagrams of the lock-in behaviour previously observed with neutron scattering and ultrasonic studies at $\boldsymbol{\tau} = \frac{1}{4}\,\boldsymbol{c}^*$ [27] and $\boldsymbol{\tau} = \frac{5}{18}\,\boldsymbol{c}^*$ [16]. These results will be discussed in terms of some theoretical expectations [21, 22] and other experimental results [10–15].

2. Experimental details

A two-axis spectrometer at the Safari-1 reactor facility of the AEC of South Africa was used for the neutron diffraction measurements. A beam of neutrons of wavelength 1.072 Å was selected with a germanium(111) monochromator. Integrated intensity measurements of the $(0, 0, 2 - \delta)$ satellite and $(0, 0, 2)$ nuclear reflection were performed as a function of temperature throughout the magnetically ordered region and with special attention to temperatures in the vicinity of the $\boldsymbol{\tau} = \frac{1}{6}\,\boldsymbol{c}^*$, $\frac{2}{11}\,\boldsymbol{c}^*$, $\frac{1}{4}\,\boldsymbol{c}^*$, and $\frac{5}{18}\,\boldsymbol{c}^*$ spin-slip structures. Use was made of $(\omega, 2\theta)$ scans with step sizes of 0.036° in ω. The a and c axes of the crystal were aligned in the scattering plane with a Huber four-circle goniometer onto which an Air Products and Chemicals model DE-202-OSP two-stage closed-cycle helium Displex refrigerator was fitted. In the vicinity of the $\boldsymbol{\tau} = \frac{1}{4}\,\boldsymbol{c}^*$ spin-slip structure some neutron scans through the $(1, 0, -\delta)$ satellite and $(1, 0, 0)$ nuclear reflection were also performed.

Ultrasonic velocity and attenuation measurements were performed using an MATEC 7700 system. Velocities were determined by a pulse-echo overlap technique while the attenuation was automatically obtained by comparison of the peak heights of two selected echoes using a logarithmic voltmeter. Valpey Fisher X-cut overtone polished quartz transducers of fundamental frequency 10 MHz were used to propagate a longitudinal wave along the c axis for measuring the C_{33} elastic constant and α_{33} attenuation coefficient. Using a Y-cut transducer a transverse wave was propagated along the b axis with the wave polarized along the c axis to yield the C_{44} elastic constant and α_{44} attenuation coefficient. Araldite standard epoxy was used as a bonding agent. Repeated transducer breakages experienced during shear measurements were overcome by sandwiching a 50 μm indium foil between the sample and the transducer [28].

The crystal was fitted to the cold finger of the Displex refrigerator through an intermediate aluminium sample stalk. Thin aluminium wire and a minimum of GE 7031 varnish were used to secure the sample to the aluminium stalk which then was screwed against an indium seal on to the copper cold finger of the cryostat. This arrangement attempted to allow unimpeded thermal expansion of the crystal. The crystal was enclosed in an aluminium hood filled with helium exchange gas.

A Lake Shore DTC-500 temperature controller using a silicon diode sensor was used for temperature control in the neutron diffraction experiments. In the ultrasonic work it was observed that the RF signal influenced the output of the Si diode sensor and a THOR S3010 controller with an Au + 0.07 at.% Fe versus chromel-P thermocouple was consequently employed in these studies. In neutron scattering measurements extending down to 5 K an Oxford 3120 flow cryostat and temperature controller using an Au + 0.07 at.% Fe versus chromel-P thermocouple were used.

In all instances specimen temperatures were measured with two calibrated Au + 0.07 at.% Fe versus chromel-P thermocouples secured on two opposite faces of the crystal. With all the cryogenic systems care was taken to thermally anchor all leads before going to the sample in order to minimize heat conduction into the system and avoid the risk of incorrect measurement of the sample temperature. An ice triple-point cell was employed to ensure a stable reference temperature during experimental runs. These runs could take up to 5 d. Data accumulation time at each temperature in the diffraction measurements took up to 60 min and up to 30 min was allowed for temperature stabilization between temperature changes to ensure that thermal equilibrium has been reached. Temperatures were controlled to a relative stability of better than ± 0.02 K and the absolute temperature measurement was within ± 0.5 K.

For investigations in applied fields up to 2.3 T a current-regulated Varian Associates V-3700 series electromagnet was used. For the ultrasonic measurements the Displex cryostat was mounted vertically on a sturdy support anchored to the yoke assembly of the magnet. The crystal was aligned with a specific crystal axis along the field direction to within 2°. For the neutron-scattering measurements the electromagnet was mounted on the two-axis diffractometer table with the field direction either along the vertical or within the horizontal plane. The dimensions of the magnet restricted measurements to the $(0, 0, 2)$ and $(1, 0, 0)$ Bragg reflections and their primary magnetic satellites $(0, 0, 2 - \delta)$ and $(1, 0, -\delta)$. Fields could be applied either parallel or perpendicular to the scattering vector. For ultrasonic measurements in fields larger than 2.3 T a superconducting magnet was used together with a cryostat of our own design.

Two Ho crystals of high purity were obtained from the Materials Preparation Centre, Ames. The crystals designated as Ho1 and Ho2 were shaped as cubes of approximate sizes 6 mm×6 mm×6 mm and had the principal a, b, and c axes perpendicular to the cube faces. A residual resistivity ratio (RRR) of $\rho_{300K}/\rho_{4K} \approx 100$ was specified for these crystals by the supplier. Ultrasonic measurements, as well as some neutron measurements, were performed on the crystals as received. However, crystal Ho1 was cut with spark erosion in the course of the investigation to provide a disc- and various pillar-shaped samples for certain neutron-scattering measurements. Geometrical details of the different samples used are given in table 2.

Table 2. Holmium crystals used in this investigation. Both crystals Ho1 and Ho2 were used in the initial neutron diffraction studies but crystal Ho1 was cut in a variety of slabs, a disc, and pillars to meet the requirements of various subsequent measurements.

		Dimensions (mm)		
Crystal	Geometry	a axis	b axis	c axis
Ho1	cube	6.25	6.45	6.20
Ho2	cube	6.30	6.48	6.11
Ho1D	disc	2.45	6.20	6.20
Ho1P2b	pillar	2.05	6.45	2.90

3. Introductory results

The temperature dependences measured in zero magnetic field of the integrated intensities from the $(0, 0, 2 - \delta)$ satellite reflection and the $(0, 0, 2)$ nuclear reflection, as well as the interlayer turn angle ω between the ferromagnetic spin layers of the helical structure, are shown in figure 1. Results are obtained during decreasing temperature runs (open symbols) and subsequent increasing temperature runs (closed symbols). This convention to indicate the direction of temperature change will be followed throughout the paper. The onset of helical magnetic ordering at $T_N = 132.15$ K is clearly evident and the critical behaviour associated with this transition has been reported in a previous publication [29]. The transition to a ferromagnetic cone structure below $T_C = 18.8$ K is clearly indicated from a cusp in the integrated intensity and in the rapid drop to a turn angle of 30°. The first-order nature of this transition is evident from hysteresis in the value of T_C as observed during cooling compared to heating runs. It is also evident that there exists appreciable hysteresis in the observed intensity values in the helical region taken during cooling followed by heating runs. Intensity

measurements were performed in all our neutron studies against a constant monitor count rate in order to negate the effects of variations in reactor power. Since a typical cooling and heating run as shown in figure 1 took in excess of 100 h we also monitored the intensity of the $(0, 0, 2)$ nuclear reflection as a further check on the long-term stability of our intensity measurements. The $(0, 0, 2)$ intensities are, apart from slight structure near T_C, observed to vary smoothly as a function of temperature and indicate no hysteresis. Thus, the large hysteresis effects indicated for the magnetic $(0, 0, 2-\delta)$ reflection in figure 1 and previously studied in detail by us [30] cannot be ascribed to instrumental sensitivity changes during these long experimental runs. It has been shown that the nature of the hysteresis in Ho is sample dependent with less pure samples (RRR $\sim$ 10) showing smaller hysteresis effects than the high-purity samples (RRR $\sim$ 100) studied here [30]. Hysteresis effects in magnetic x-ray-scattering studies [8, 9] and in neutron-scattering investigations [10, 11] have been reported for Ho at low temperature and may be associated with the series of first-order transitions associated with the succession of supercommensurate structures found in Ho with a decrease in temperature. We took cognizance of the possibility of hysteresis in our experimental work by making all measurements described in this paper by slowly cooling down from the paramagnetic region in the first instance. Subsequently results were taken during a heating run which always ended at least 15 K higher than T_N before a next cooling run was attempted. Temperatures were nevertheless regulated at fixed points during these cooling or heating runs as described in section 2.

The turn angle ω as observed from the relative positions of the $(0, 0, 2-\delta)$ satellite and the $(0, 0, 2)$ nuclear peak is depicted in figure 1(B). The two Bragg peaks were fitted with a Gaussian function rendering an accuracy of $\pm 0.01^\circ$ in the position of a peak. A smooth monotonic decreasing curve for ω is obtained over the complete temperature region with a rather rapid fall in the region just above T_C to a value of 30° at and below T_C.

The zero-field temperature dependences for decreasing and increasing temperatures of the elastic constant C_{44} are indicated in figures 2(A) and (B) respectively together with the attenuation coefficient α_{44}. The onset of helical ordering at T_N leads to an additional contribution $\Delta C_{44} = C^m_{44}(T) - C^0_{44}(T)$, where $C^m_{44}(T)$ is the measured constant and $C^0_{44}(T)$ is the contribution expected from the non-magnetic crystal. The magnetic contribution ΔC_{44}, as we have indicated previously for a dysprosium crystal [31], scales rather well with the square of the sublattice magnetization m_n of the helical magnet as measured through the intensity of neutron scattering, $I \sim m_n^2$. Apart from distinct but small anomalies at 97.5 K where $\boldsymbol{\tau} = \frac{1}{4}\,\boldsymbol{c}^*$, and at low temperatures in the vicinity of T_C, the temperature dependence of C_{44} in the helical region is given by very smooth curves as indicated in figure 2. It is also remarkable that there is, except for hysteresis behaviour associated with the aforementioned small anomalies at 97.5 K and near T_C, no other evidence of hysteresis when comparing the global $C_{44}(T)$ curves obtained during cooling and heating runs. This suggests that $\Delta C_{44}(T)$ could be a clearer indication of the magnetic order parameter in the helical region than the temperature dependence of an individual magnetic reflection such as the $(0, 0, 2-\delta)$ satellite.

The global behaviours indicated for Ho in figures 1 and 2 are in agreement with previously reported results of turn angle [8, 17], the cusp near T_C in satellite neutron intensities [17], and results of C_{44} [32–34] and α_{44} [34] measurements. The temperature dependence of C_{44} at low temperatures as shown in the insets to figure 2 is of interest. Earlier elastic constant measurements on Ho [32, 33] only indicated anomalies near 25 K and at T_C ($\approx$18 K), but measurements by Bates *et al* [11] indicate that, in addition to these anomalies, the C_{33}, C_{44}, C_{11}, and C_{66} elastic constants exhibit small but distinct anomalies at a temperature of 2 K above T_C. The latter anomalies are associated with the $b = 11$ spin

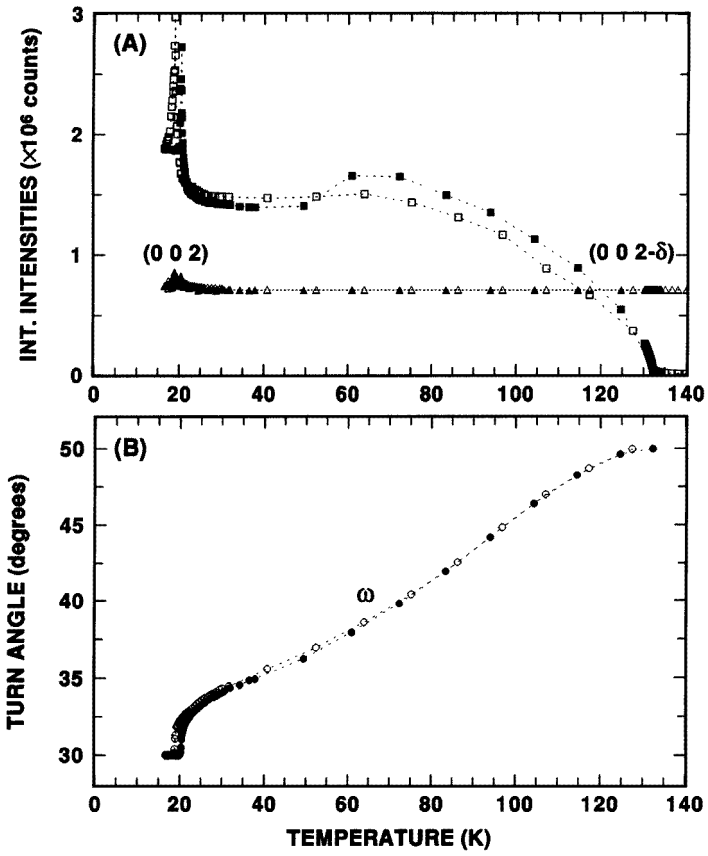

Figure 1. Neutron diffraction results observed in transmission using crystal Ho1D depicting the temperature dependence of (A) the integrated intensities from the $(0, 0, 2-\delta)$ satellite reflection and the $(0, 0, 2)$ nuclear reflection and (B) the interlayer turn angle ω. Open symbols refer to decreasing and closed symbols to increasing temperature runs.

slip of monoclinic magnetic symmetry [11]. Whereas the magnitude of the dip obtained by us in C_{44} at 24 K is comparable to that observed by Bates *et al*, the size of the additional anomaly observed in C_{44} for our crystal near T_C is about half of that found by Bates *et al*. The temperature dependence of the elastic constant C_{33} is used in section 8 to delineate the $\boldsymbol{\tau} = \frac{5}{18}\,\boldsymbol{c}^*$ lock-in region in a *b*-axis-directed field. In section 9 both C_{33} and C_{44} measurements are reported for the complete magnetic region of Ho and used to construct a tentative phase diagram for spin-slip behaviour as a function of *b*-axis-applied field.

4. Turn angle lock-in with *b*-axis-directed fields at low temperature

The temperature dependences of turn angle ω and integrated intensities for the $(0, 0, 2-\delta)$ and $(0, 0, 2)$ reflections measured in zero magnetic field and for some other representative values of field B are shown in figure 3. The measurements in zero field were performed in transmission mode on the disc-shaped crystal Ho1D (figure 3(A)), while the results depicted in figure 3(B–D) were obtained also in transmission using the pillar-shaped crystal Ho1P2b. An experimental run in $B = 0.2$ T using crystal Ho1D (not shown) gave essentially the

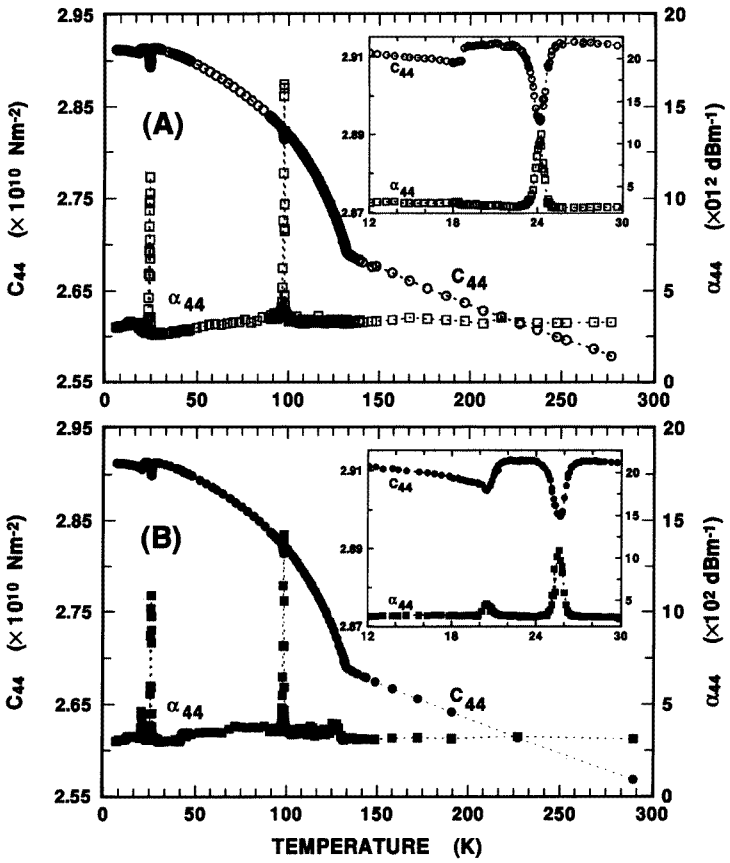

Figure 2. The temperature dependence of the shear elastic constant C_{44} and attenuation coefficient α_{44} measured on crystal Ho2 by propagating shear waves along the b axis with polarization along the c axis during (A) a decreasing temperature run and (B) an increasing temperature run.

same results as depicted in figure 3(B) for crystal Ho1P2b, thus indicating negligible effects of demagnetization corrections in these experiments.

The results are in agreement with the more limited set of measurements by Pearce *et al* [17] who reported a lock-in to $\boldsymbol{\tau} = \frac{2}{11}\,\boldsymbol{c}^*$ in their b-axis-directed field of 0.03 T and observed cusps in the integrated intensities at temperatures where the interplanar turn angle exhibits steps. The cusps are ascribed by Pearce *et al* [17, 35] as due to extinction effects associated with the magnetic lattice. It is evident from figure 3(B) that a clear lock-in is obtained for $\omega = 32.7^\circ$ corresponding to $\boldsymbol{\tau} = \frac{2}{11}\,\boldsymbol{c}^*$ for our b-axis-directed field of $B = 0.2$ T. A well defined lock-in was also observed for $B = 0.1$ T (not shown). At higher applied fields the extent of the plateau region becomes less clear, presumably signifying the admixture of phases with other wave vectors into the $\boldsymbol{\tau} = \frac{2}{11}\,\boldsymbol{c}^*$ region.

One observes in figure 3(C) and (D) that the wave vector for these values of applied field lock into values for $\boldsymbol{\tau} < \frac{1}{6}\,\boldsymbol{c}^*$ at the lowest temperatures. An appreciable intensity increase of the $(0, 0, 2)$ nuclear reflection is also evident in figure 3(C) and (D) at low temperatures. The minimum turn angle values observed for the magnetic structure at the lowest attainable temperatures as a function of the magnitude of the b-axis-directed field

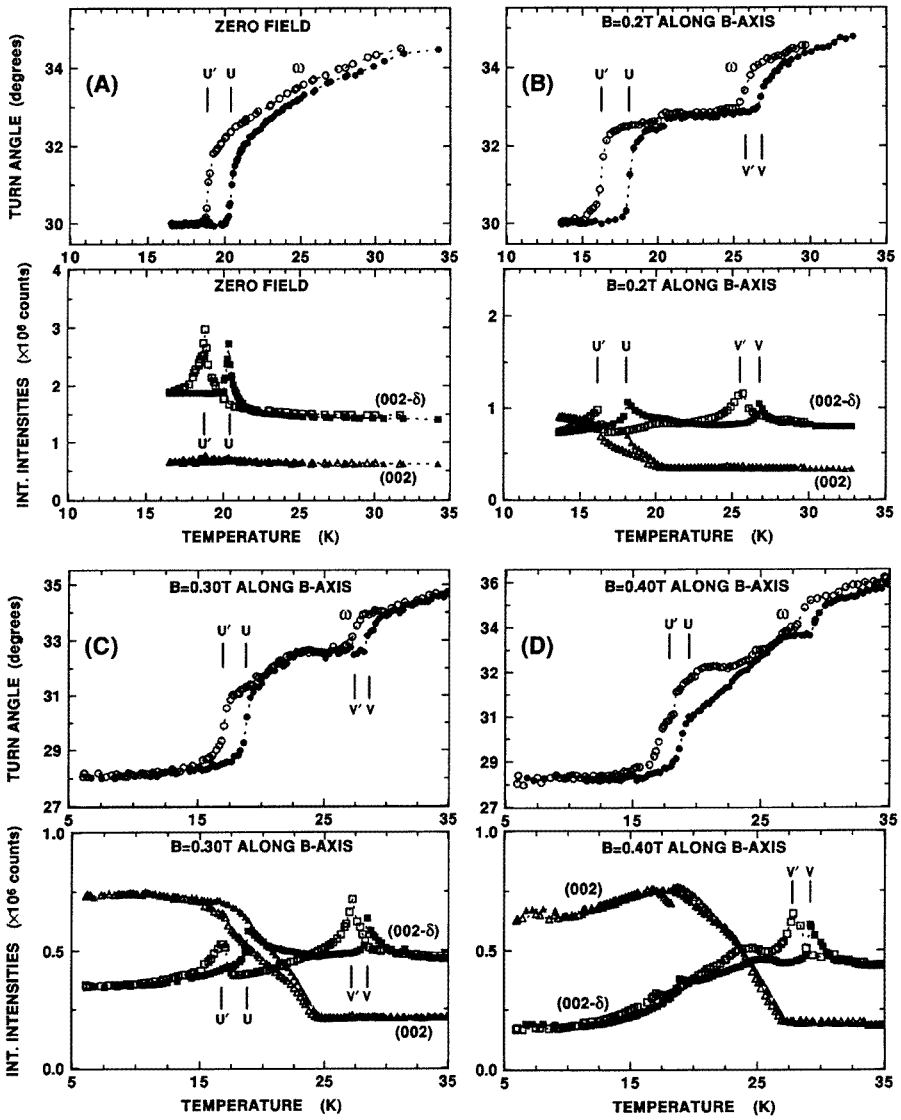

Figure 3. Temperature dependences of turn angle ω and integrated intensities for the $(0, 0, 2-\delta)$ and $(0, 0, 2)$ reflections measured in zero field and for various values of field B: (A) crystal Ho1D; (B)–(D) crystal Ho1P2b. In all cases measurements were performed in transmission. Open symbols refer to decreasing and closed symbols to increasing temperature runs. Field-induced lock-in to $\boldsymbol{\tau} = \frac{2}{11}\,\boldsymbol{c}^*(\omega = 32.7^\circ)$ is clearly evident for $B = 0.2$ T applied along the b axis. Phase boundaries associated with steps in ω and cusps in the integrated intensity are indicated by U′, U, V′, and V.

are indicated in figure 4. The turn angle passes through a minimum value of approximately 28° and then return to a value of 30° for $B \geqslant 0.5$ T.

A phase diagram that indicates the extent of the temperature regimes in which the spins lock into $\boldsymbol{\tau} = \frac{1}{6}\,\boldsymbol{c}^*$ and $\boldsymbol{\tau} = \frac{2}{11}\,\boldsymbol{c}^*$ when the field is applied along the b axis is given as figure 5. This diagram has been compiled by considering the temperatures where steps in

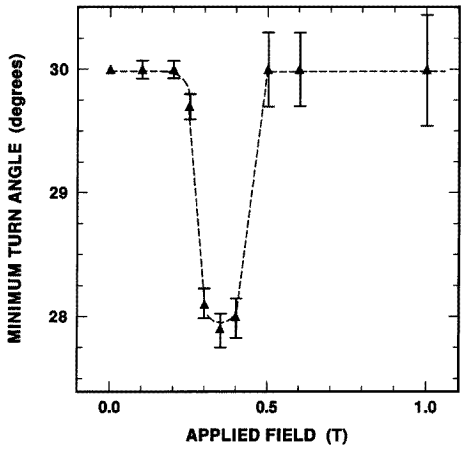

Figure 4. The minimum turn angle observed as a function of *b*-axis-directed field in the low-temperature conical ferromagnetic phase of Ho.

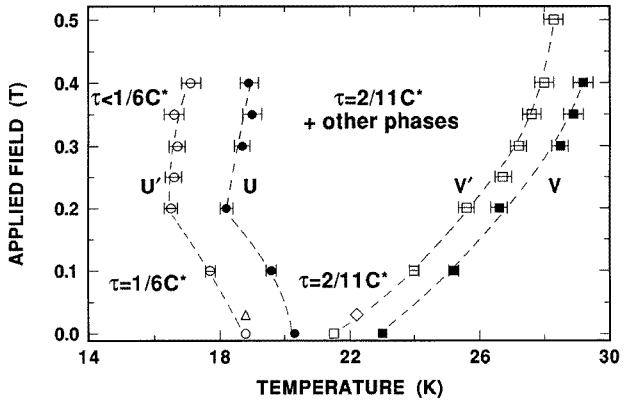

Figure 5. A phase diagram indicating the extent of the temperature regimes in which the spins lock into $\tau = \frac{1}{6}\ c^*$ and $\frac{2}{11}\ c^*$ structures with field applied along the *b* axis of Ho. Both steps in ω and cusps in the intensity curves as indicated in figure 3 with the letters U′, U, V′, and V were used to construct the diagram. The dashed lines are a guide to the eye with lines U′ and V′ indicating results from cooling runs and U and V results from heating runs.

turn angle and cusps in the intensity curves occur as indicated by the letters U′, U, V′, and V in figures 3 and 5. The primed letters are associated with cooling runs and the unprimed letters with the results of heating runs.

5. The influence of *c*-axis-directed fields on ω at low temperature

Turn angles and integrated intensities for the $(0, 0, 2 - \delta)$ satellite at low temperatures are given in figure 6 for cooling followed by heating runs for *c*-axis-directed fields. For $B \leqslant 0.9$ T one observes that values for the lock-in of turn angle observed at the lowest temperatures increase approximately linearly from $\omega = 30^\circ$ in zero field to 30.6° in $B = 0.9$ T as indicated in figure 7. Of further interest is that at higher fields the turn

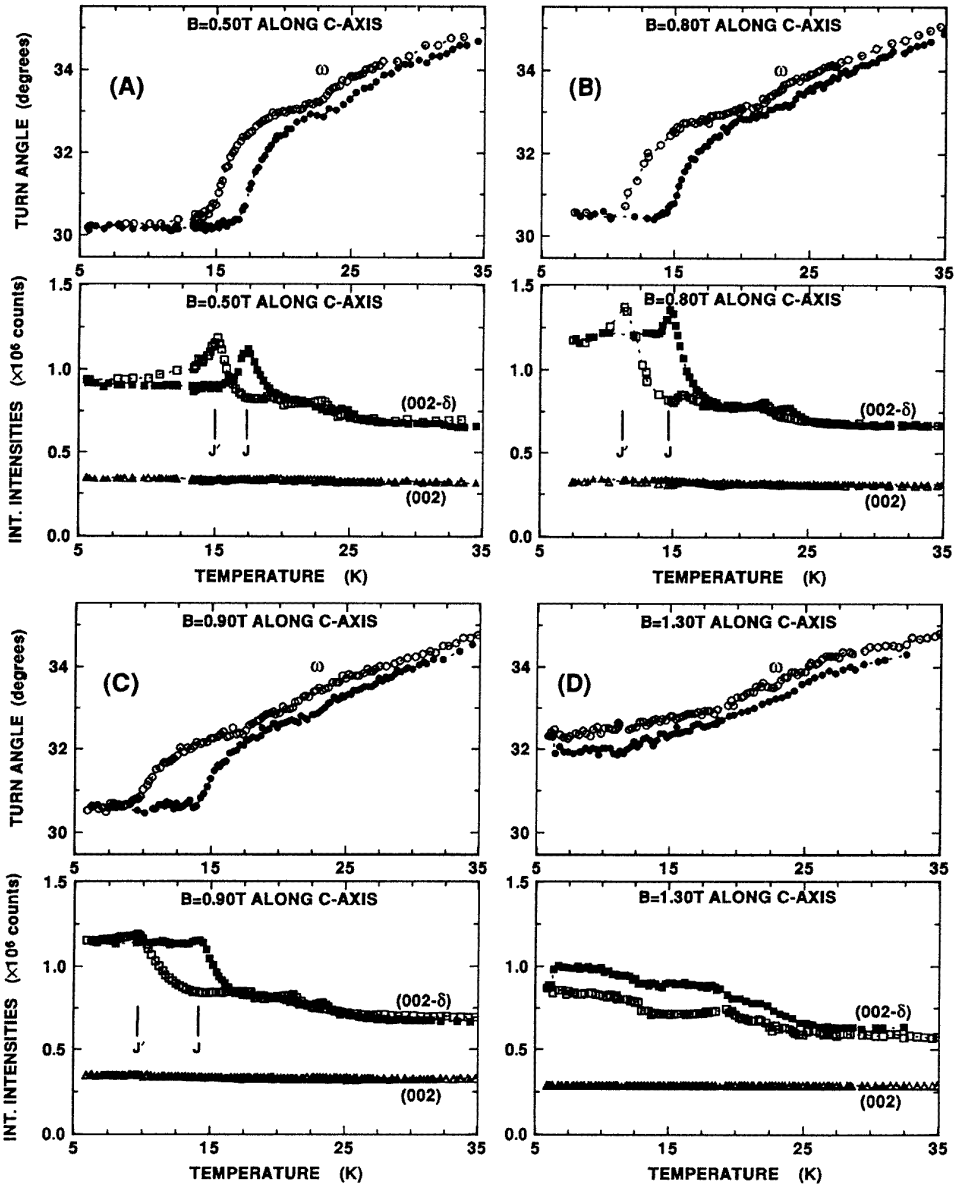

Figure 6. Temperature dependences of turn angle and integrated intensity for the $(0, 0, 2 - \delta)$ satellite measured in transmission for cooling (open symbols) followed by heating runs (closed symbols) with field applied along the c axis of crystal Ho1D. Temperatures where cusps appear in the integrated intensities are indicated by J′ (cooling runs) and J (heating runs) and used to construct the phase diagram of figure 8.

angle tends to lock into $\omega \approx 32^\circ$ at the lowest temperature, indicating the predominance of the $\boldsymbol{\tau} = \frac{2}{11}\,\boldsymbol{c}^*$ structure. This result agrees with the finding of Cowley *et al* [18] which indicates that with an increasing c-axis-directed field at low temperature the wave vector assumes a value of $\boldsymbol{\tau} = \frac{2}{11}\,\boldsymbol{c}^*$ at 2 T followed by further values of $\boldsymbol{\tau} = \frac{3}{16}\,\boldsymbol{c}^*$, $\frac{4}{21}\,\boldsymbol{c}^*$,

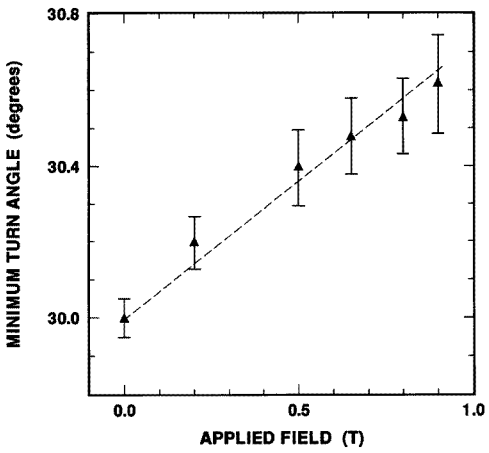

Figure 7. Minimum turn angle values observed at the lowest attainable temperatures for fields applied along the c axis.

and $\frac{5}{26}\ \boldsymbol{c}^*$ of the devil's staircase at higher fields. For fields $B \leqslant 0.9$ T we identify the temperatures at which the cusps in the integrated intensities of the $(0, 0, 2-\delta)$ satellite occur with symbols J′ and J in figure 6. These values are used to construct a phase diagram for the c-axis-directed field for both decreasing and increasing temperature runs in figure 8. Regions are indicated where the wave vectors $\boldsymbol{\tau} = \frac{1}{6}\ \boldsymbol{c}^*$ and $\boldsymbol{\tau} = \frac{2}{11}\ \boldsymbol{c}^*$ are dominant.

6. Lock-in behaviour at the supercommensurate $\boldsymbol{\tau} = \frac{1}{4}\ \boldsymbol{c}^*$ spin-slip structure

Neutron-scattering studies in zero magnetic field of the primary magnetic satellites of helically ordered Ho, Dy, and Tb were performed by Baruchel and coworkers [36, 37] in the mid 1980s in order to search for a plateau or jump in turn angle ω associated with commensurability. No such effects were found except that the $\omega(T)$ curve of Ho showed points of inflection at $\omega = 36$ and 45°. High-resolution measurements at a wavelength of 4 Å near $\boldsymbol{\tau} = \frac{1}{4}\ \boldsymbol{c}^*$ clearly indicated an inflection point in the $\omega(T)$ curve at 97.5 K [37]. Observation of the field-induced lock-in of the wave vector was first observed in Ho at $\boldsymbol{\tau} = \frac{1}{4}\ \boldsymbol{c}^*$ and later also at $\boldsymbol{\tau} = \frac{1}{5}\ \boldsymbol{c}^*$, $\frac{5}{18}\ \boldsymbol{c}^*$, and $\frac{2}{9}\ \boldsymbol{c}^*$ by Tindall, Steinitz, and coworkers as discussed in section 1. The Chalk River group observed lock-in at $\boldsymbol{\tau} = \frac{1}{4}\ \boldsymbol{c}^*$ for a 3 T c-axis-directed field with the plateau extending over 1.8 K and for a 3 T b-axis-directed field with a smaller plateau region of 1 K [13]. These results were obtained by measuring the positions in reciprocal space of the $(1, 0, 0)$ nuclear reflection and its associated $(1, 0, \delta)$ satellite.

Our neutron-scattering experiments were restricted to fields not exceeding 2.3 T. The field was effectively applied along the c axis while scanning through the $(0, 0, 2)$ and $(0, 0, 2-\delta)$ reflections and along the b axis during a scan through the $(1, 0, 0)$ and $(1, 0, -\delta)$ reflections. In figure 9 the temperature dependences of ω as obtained from the different measurements are plotted. In figure 9(A) the temperature dependence of the turn angle in zero field is depicted for values of ω around 45°. No evidence of a lock-in is observed but some indication of an inflection point near 98 K is found. Figure 9(B) indicates the lock-in observed near 101 K with the field directed along the b axis for both decreasing and increasing temperature runs. In figure 9(C) we depict the results obtained with the c-axis-

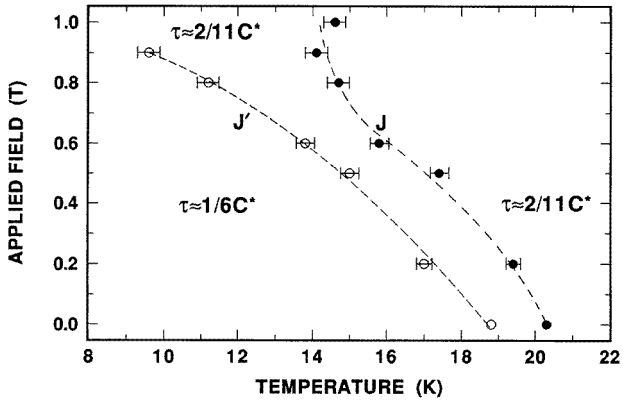

Figure 8. The field dependence of the temperatures where cusps in the integrated intensities of the $(0, 0, 2-\delta)$ satellite reflection occur for c-axis-directed fields. Results of both decreasing (open circles, J′) and increasing (closed circles, J) temperature measurements are given. The dashed lines serve as guides to the eye and separate regions where the wave vectors $\tau = \frac{1}{6}\ c^*$ and $\tau = \frac{2}{11}\ c^*$ are dominant.

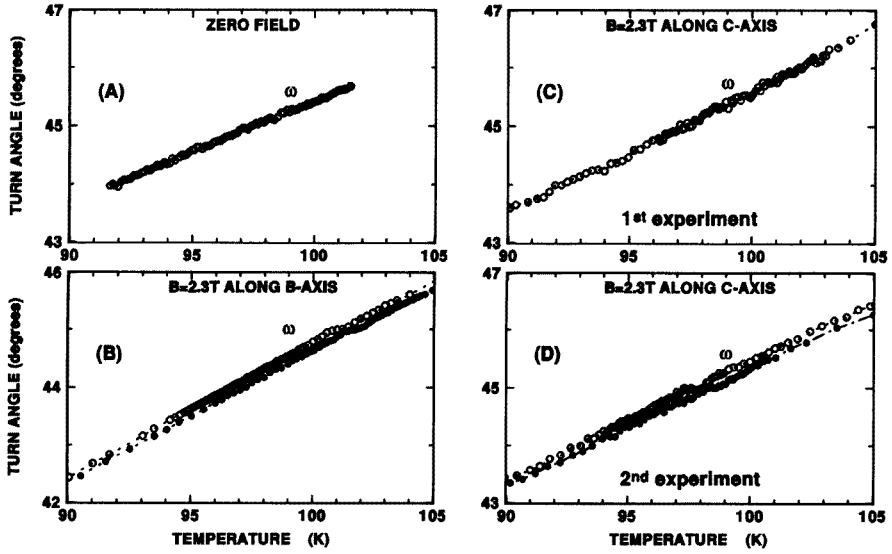

Figure 9. The temperature dependence of turn angle in order to investigate lock-in behaviour associated with the $b = 2$ spin-slip structure: (A) for zero field, (B) with $B = 2.3$ T directed along the b axis, (C) and (D) two separate experiments with $B = 2.3$ T directed along the c axis as described in the text. Experiments were performed on crystal Ho1. Open circles refer to decreasing and closed circles to increasing temperature runs.

directed field during a cooling run performed in 1992 [27]. No evidence was indicated for the existence of a lock-in from the measurements. The results of this study are in contrast with the Chalk River results on another Ho crystal [12, 13]. On the other hand, as discussed in section 1, theoretical work by Plumer [21] indicated lock-in behaviour to be expected for b-axis-directed fields but not for c-axis-directed fields. The investigation was further

pursued with a second experiment on the same Ho1 crystal. This experiment indicated lock-in (near 98 K) for both decreasing and increasing temperature runs in a c-axis-directed field as shown in figure 9(D). A possible explanation for the different results obtained in the two separate experiments may be found in the theoretical work by Jensen [22]. The inclusion of a trigonal coupling in his mean-field calculations results in an induced ferromagnetic moment in the basal plane when $\boldsymbol{\tau} = \frac{1}{4}\,\boldsymbol{c}^*$. If the field is aligned exactly along the c axis no appreciable lock-in is expected but the lock-in temperature interval ΔT increases rapidly as the field is moved away from the c axis by an angle θ, e.g. ΔT is calculated to be 2.7 K at $\theta = 1^\circ$ for $B = 3$ T. With a field of 3 T applied along the b axis a fan structure is probably induced and a lock-in interval of $\Delta T \approx 1$ K is predicted. It is difficult to align the magnetic field to better than within 2° from the c axis in our experiments. It is conceivable that in the experiment depicted in figure 9(C) the field direction was fortuitously so close to the c axis while the diffractometer scanned through the $(0, 0, 2-\delta)$ peak that no plateau in ω was observed. For the second experiment (figure 9(D)) and in the Chalk River experiments, the observed lock-in for the c-axis-directed field may have occurred due to small misalignment between the field direction and c axis while scanning through the magnetic satellite peak. It would be of interest to study the $\boldsymbol{\tau} = \frac{1}{4}\,\boldsymbol{c}^*$ lock-in effects in Ho for fields directed with different orientations in the bc plane of the crystal. At 30° away from the c axis a value $\Delta T \sim 12$ K is predicted for a field of 3 T for the helical ordered structure. For the fan structure ΔT is likewise predicted to be large at intermediate angles between b and c axes, e.g. with a field of 3 T directed at 35° away from the b axis, $\Delta T \sim 8$ K.

7. Phase diagrams for the $\boldsymbol{\tau} = \frac{1}{4}\,\boldsymbol{c}^*$ structure

Associated with the lock-in an anomalous behaviour of the integrated neutron intensities of the $(1, 0, \delta)$ satellite has been observed in the temperature region near $\boldsymbol{\tau} = \frac{1}{4}\,\boldsymbol{c}^*$ [12, 13]. It comprises a rise–fall–rise behaviour of the intensity as the temperature is changed through the lock-in region for both c-axis and b-axis-directed fields [13]. This behaviour has also been observed in our measurements as indicated in figure 10(D) for the $(1, 0, -\delta)$ satellite observed with a 2.3 T b-axis-directed field. This feature is furthermore also characteristic of the behaviour at the $\boldsymbol{\tau} = \frac{1}{5}\,\boldsymbol{c}^*$ [13] and $\boldsymbol{\tau} = \frac{2}{9}\,\boldsymbol{c}^*$ [15] lock-ins, but its origin is not as yet understood. We indicate in figure 10(C) that for the $(0, 0, 2-\delta)$ satellite and with the field applied along the c axis the field-induced intensity anomaly occurs as a simple dip in the intensity rather than the more complicated rise–fall–rise structure. A dip in intensity may originate from increased extinction due to a more perfect structure in the supercommensurate lock-in region, but this argument will not account for the increase in intensity at either end of the lock-in region observed for the $(1, 0, \delta)$ satellite [13].

Our ultrasonic investigations on the high-purity Ho2 crystal extend previous studies [28, 38–40] of anomalies in C_{44} and α_{44} associated with the $\boldsymbol{\tau} = \frac{1}{4}\,\boldsymbol{c}^*$ structure. Specifically we investigate both C_{44} and α_{44} for magnetic fields applied along the principal a, b, and c directions. Furthermore, the hysteresis in the temperature at which these anomalies occur during cooling or heating runs, which was mentioned by Simpson *et al* [28], is studied in detail by us. Some of our results have been presented previously [41], but our measurements have subsequently been extended to higher fields. In figure 11 we depict results for a few selected temperature runs through the transition in zero field and with the field B along the b or the c axis. Within the accuracy of the measurements the minimum in C_{44} and maximum in α_{44} for a specific field are observed to occur at the same temperature. Hysteresis in the location of the anomaly is clearly evident from results observed during cooling (open symbols) and during heating (closed symbols). The magnitudes of the zero-field anomalies

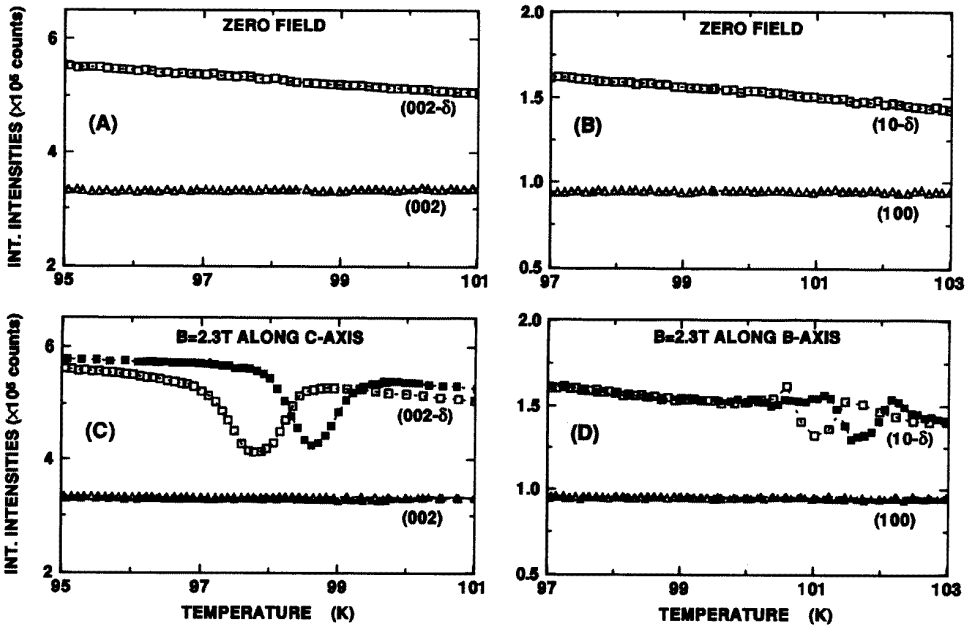

Figure 10. Anomalous intensity behaviour associated with the $b = 2$ spin-slip structure for the $(0, 0, 2 - \delta)$ satellite reflection with a c-axis-directed field and for the $(1, 0, -\delta)$ satellite reflection with a b-axis-directed field. Measurements were taken on the Ho1 crystal. Open and closed symbols refer respectively to cooling and heating runs.

in C_{44} and α_{44} (figure 11(A)) are significantly reduced with increase in B as indicated for the b-axis-directed field in figures 11(B) and (C) and for the c-axis-directed field in figure 11(D). Application of the field along the b axis significantly moves the position of the anomalies to higher temperature, whereas only a small effect is obtained with the field directed along the c axis.

Neutron-scattering measurements have thus far not been able to establish the possible temperature width of the commensurate region in zero field associated with the $b = 2$ spin slip [36, 37], (see also figure 9(A)). Hence the width associated with the C_{44} anomaly in $B = 0$ in figure 11(A) does not necessarily reflect a finite lock-in for the zero-field case. On the other hand in an applied field lock-in effects are observed through both wave-vector plateaus and anomalies in scattered neutron intensities. In principle one should therefore be able to obtain from these experiments the width of the lock-in region as a function of magnetic field. This would then lead to two branches in a (B, T) phase diagram for the $b = 2$ spin-slip transition indicating respectively the two first-order transitions that are expected to bracket the lock-in region [21]. In practice wave-vector measurements have not demonstrated the expected discontinuity in τ at the expected two first-order transitions. In view of these considerations we took the pragmatic viewpoint in constructing our phase diagram of using the minima in C_{44} and maxima in α_{44} from the ultrasonic studies and the minima in the neutron intensity curves as presumably representing in applied fields the mid-point of the lock-in region. It is noted that the small C_{44} anomaly resides on a fairly steeply changing 'background' curve, leading to an asymmetrical shape for the anomaly. It has been verified, by plotting the difference between a linear background and the measured points as function of temperature, that the position of the minimum obtained in this way does

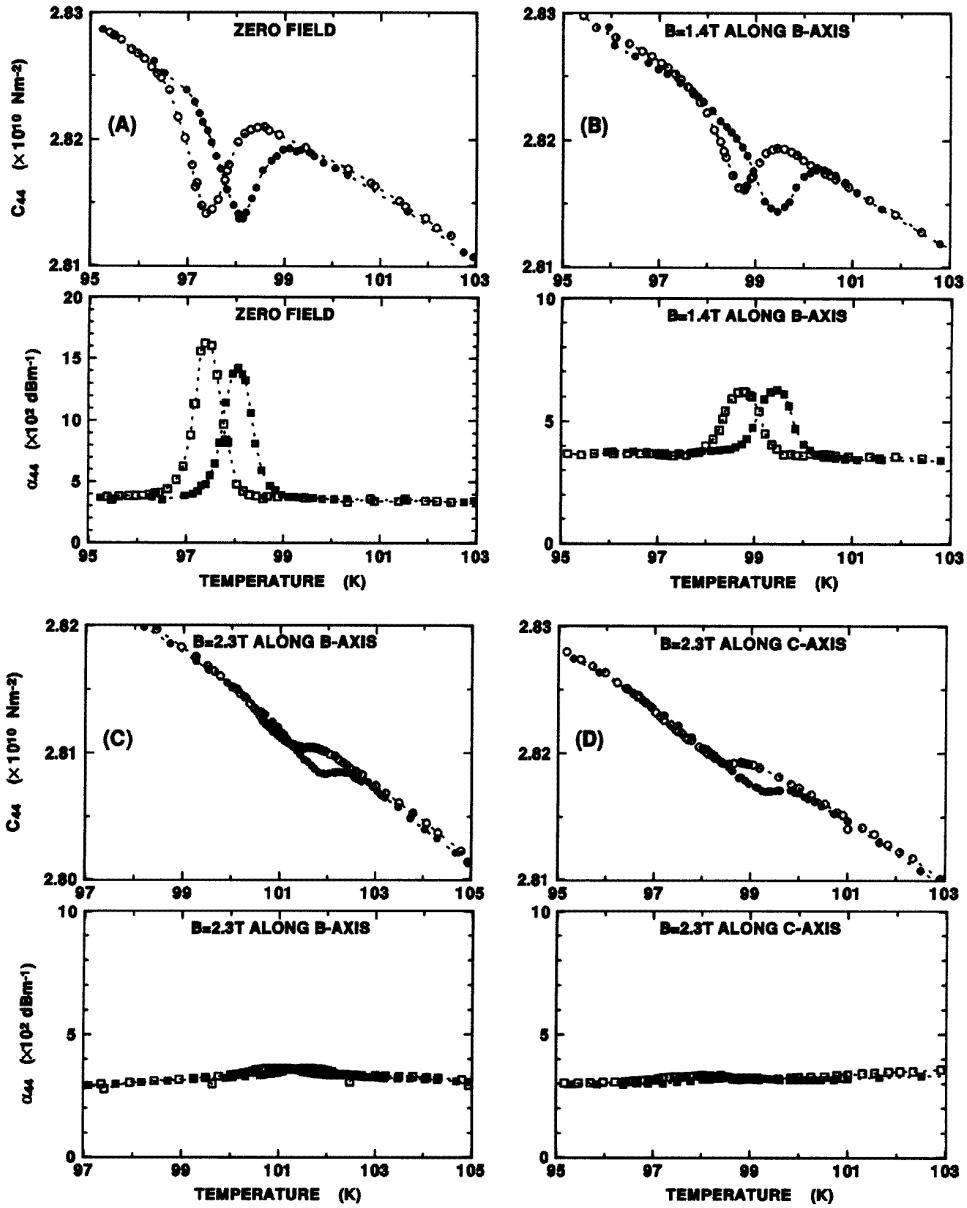

Figure 11. Anomalies in C_{44} and α_{44} and measured on crystal Ho2 in zero field and with fields directed along either the b axis or the c axis in order to study the $b = 2$ spin-slip structure. Open and closed symbols refer respectively to cooling and heating runs.

not noticeably differ from that observed directly from figure 11. In figure 12 a (B, T) phase diagram for the $\tau = \frac{1}{4}\,c^*$ structure of Ho as obtained from ultrasonic and neutron-scattering measurements is given for fields applied along both b and c axes. It is observed that in spite of the aforementioned discussed differences between the ultrasonic- and neutron-monitored effects there nevertheless seems to be correspondence between the temperature dependence

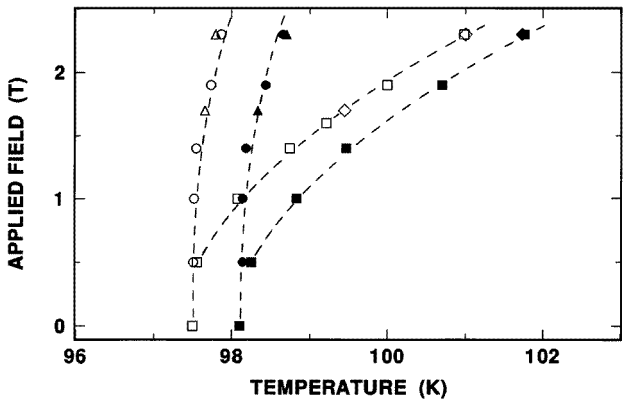

Figure 12. A phase diagram for the $b = 2$ spin-slip structure of Ho as derived from the results given in figures 10 and 11 and ultrasonic runs at other field strengths: neutron intensity minima for B parallel to the c axis (△, ▲) and with B parallel to the b axis (◇, ♦); ultrasonic anomalies with B parallel to the c axis (○, ●) and with B parallel to the b axis (□, ■). Open and closed symbols refer respectively to cooling and heating runs.

of the anomaly in the neutron intensity and that of the C_{44} anomaly. One also notes that the effect of a b-axis-directed field is much more pronounced than that with the field directed along the c axis.

For the field directed along the a axis the ultrasonic behaviour is complex, namely, as indicated for two representative fields in figure 13, a splitting of the initial zero-field anomalies in C_{44} and α_{44} takes place. This leads to the intricate phase diagrams of figure 14 in which the two minima observed in C_{44} and two maxima observed in α_{44} give somewhat different phase diagrams as depicted respectively in figures 14(A) and (B).

8. Lock-in behaviour at the $\tau = \frac{5}{18}$ c* structure

A lock-in at $\boldsymbol{\tau} = \frac{5}{18}\ \boldsymbol{c}^*$ has been observed from neutron scattering by Tindall *et al* [13, 14] between 126 K and $T_N \approx 132.9$ K when applying a field of 3 T along the b axis. We have verified the finding of the Chalk River group by performing neutron diffraction measurements. Rocking curves of the $(1, 0, 0)$ and $(1, 0, -\delta)$ Bragg reflections with their centres determined by Gaussian fits yield values of wave vector $\boldsymbol{\tau}$ as a function of temperature. The results observed on crystal Ho1D with fields of 1.5 and 2.3 T applied along the b axis corroborate the previous finding at Chalk River that lock-in occurs at $\boldsymbol{\tau} = \frac{5}{18}\ \boldsymbol{c}^*$ over a finite temperature interval extending from T_N to below. The lower temperatures where the lock-in sets in at 1.5 and 2.3 T are depicted in figure 16 and will be discussed below in relation to our ultrasonic results.

Results for the C_{33} elastic constant and the α_{33} attenuation coefficient measured on crystal Ho2 are depicted in figure 15. It is observed that the marked step in the zero-field value of C_{33} at T_N (indicated by Z in figure 15) is upon application of a b-directed field reduced in magnitude, followed by a plateau and a second step (indicated by Y) at lower temperature. Two well defined attenuation peaks coincide with the positions of the steps. Application of higher fields increases the width of the plateau, but the height of the second step and the magnitude of both attenuation peaks are appreciably reduced at the maximum field of 2.3 T. The phase transition at T_N has previously been observed as not

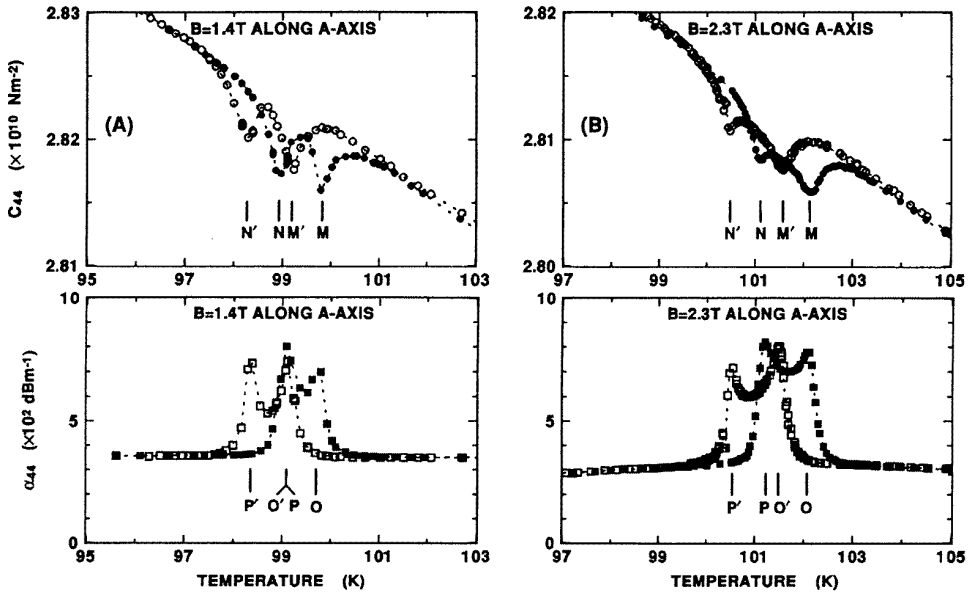

Figure 13. Anomalies in C_{44} and α_{44} measured on crystal Ho2 in fields directed along the a axis are presented in view of studying the $b = 2$ spin-slip structure. For C_{44}, in a cooling run (open symbols) two minima M′ and N′, and in a heating run two minima N and M, occur as indicated. The attenuation maxima occur at O′ and P′ (cooling) and at P and O (heating).

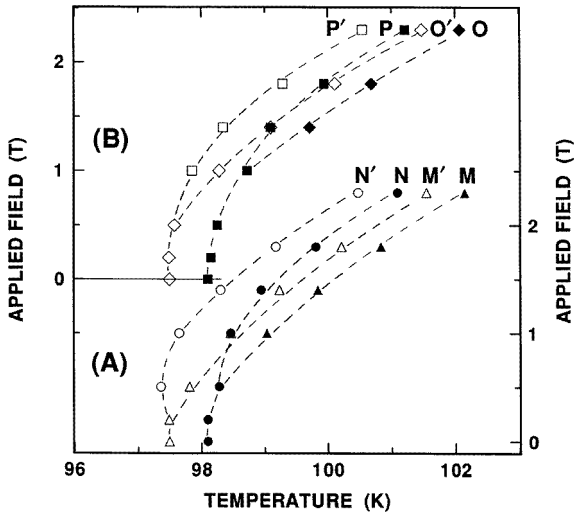

Figure 14. Phase diagrams for the $b = 2$ spin-slip structure of holmium with fields along the a axis as derived from the results given in figure 13 and also using ultrasonic measurements taken at other field strengths. Use was made in (A) of minima in $C_{44}(T, H)$ and in (B) of maxima in $\alpha_{44}(T, H)$ with the anomalies labelled as in figure 13.

exhibiting hysteresis and it is also observed that the second anomaly at lower temperature seems to be hysteresis free. The temperatures at which the ultrasonic anomalies occur are

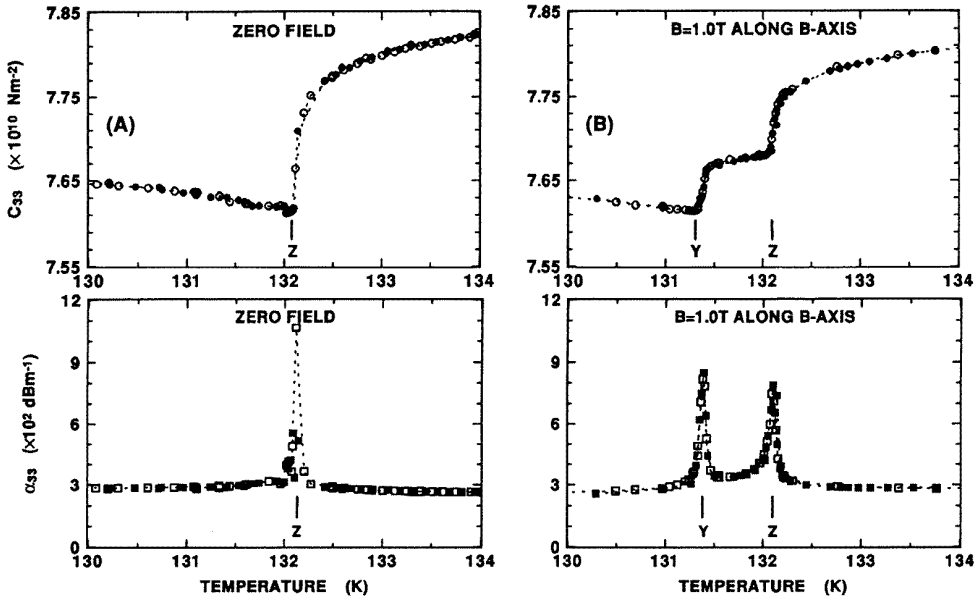

Figure 15. Anomalies in the elastic constant C_{33} and attenuation coefficient α_{33} which are associated with the $\tau = \frac{5}{18}\ c^*$ lock-in observed with basal-plane-applied fields as described in the text. Anomalies are observed at T_N (indicated by Z) and also at a lower temperature when a field is applied (indicated by Y). No temperature hysteresis is observed between the results of decreasing (open symbols) and increasing (closed symbols) temperature runs.

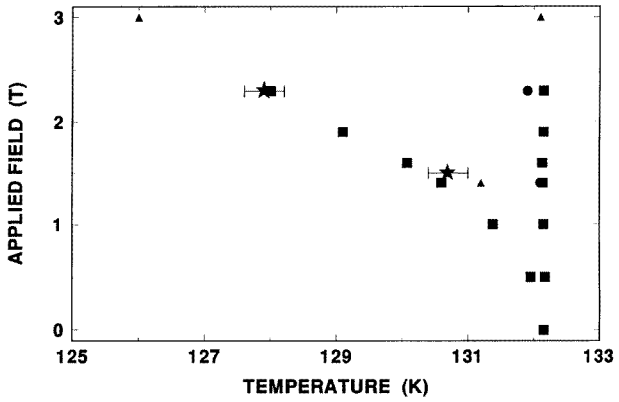

Figure 16. The extent of the $\tau = \frac{5}{18}\ c^*$ lock-in region for fields applied along the b axis of Ho as observed with neutron diffraction measurements (▲, Tindall *et al*; ★, this investigation) and our ultrasonic measurements (■). The effect of a c-axis-directed field on T_N is also indicated (○). Error bars are appended to our neutron diffraction measurements, while the size of the symbols is of the order of the error in our ultrasonic measurements.

plotted in figure 16 as squares and no distinction is made between cooling and heating runs. Comparing the results of our neutron measurements, which give the width of the $\tau = \frac{5}{18}\ c^*$ lock-in region (denoted by stars), and the ultrasonic results indicates that the lower-temperature step in C_{33} and the corresponding α_{33} peak are clear indicators of the

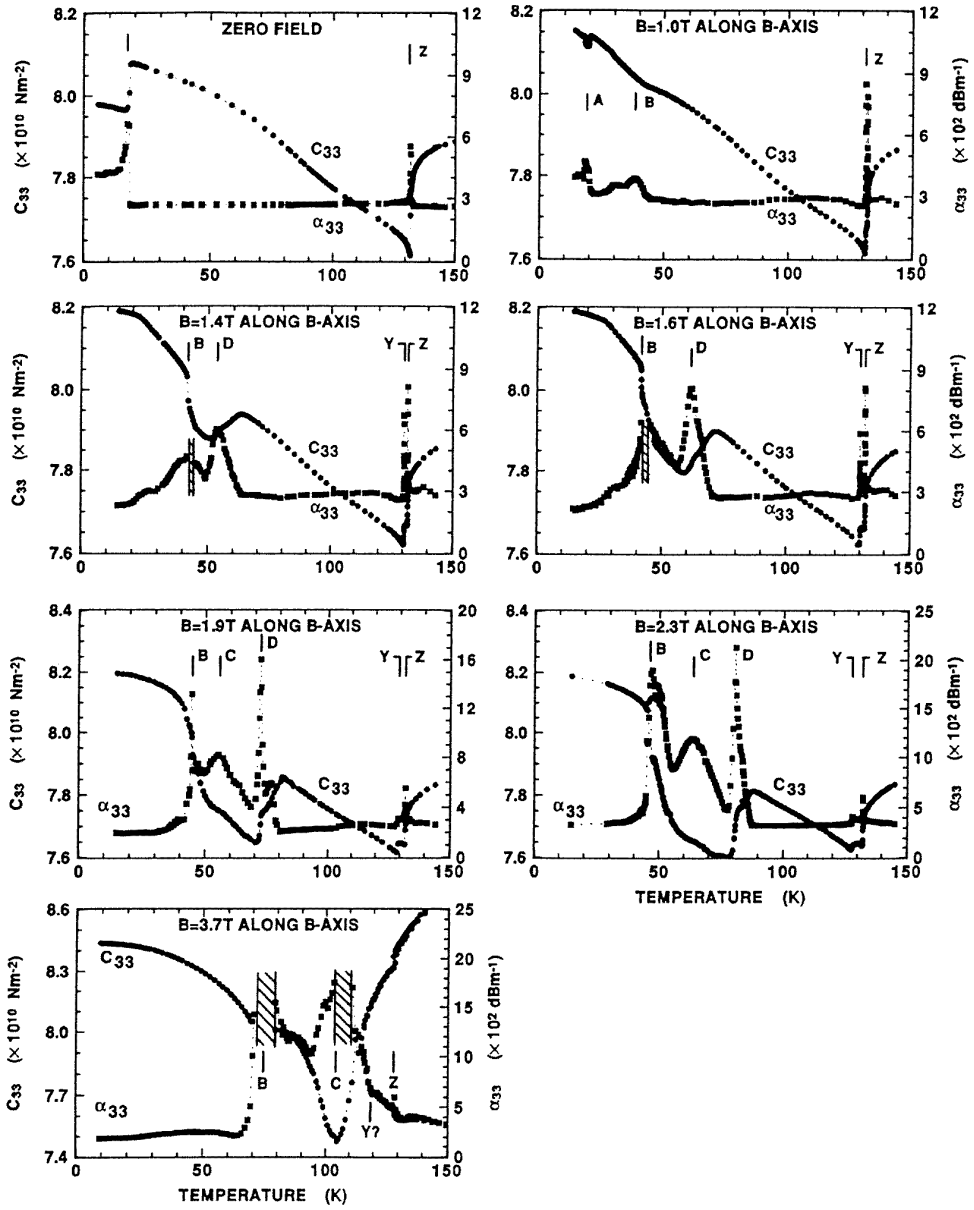

Figure 17. The temperature dependence of the compressive elastic constant C_{33} and associated attenuation coefficient α_{33} measured on crystal Ho2 during increasing temperature runs. Isofield measurements as indicated were performed with the field directed along the *b* axis. Special features on the C_{33} or α_{33} curves are indicated with short vertical lines and denoted with letters A, B, C, D, Y, and Z. Temperatures where these features appear are plotted in figure 19, giving rise to similarly marked branches on our phase diagram.

temperature at which the $\tau = \frac{5}{18}\,\boldsymbol{c}^*$ lock-in occurs. Hence, ultrasonic measurements have been used to obtain additional points on the phase diagram for the $\tau = \frac{5}{18}\,\boldsymbol{c}^*$ lock-in as indicated in figure 16. Measurements of C_{33} and α_{33} with fields directed along the *a* axis

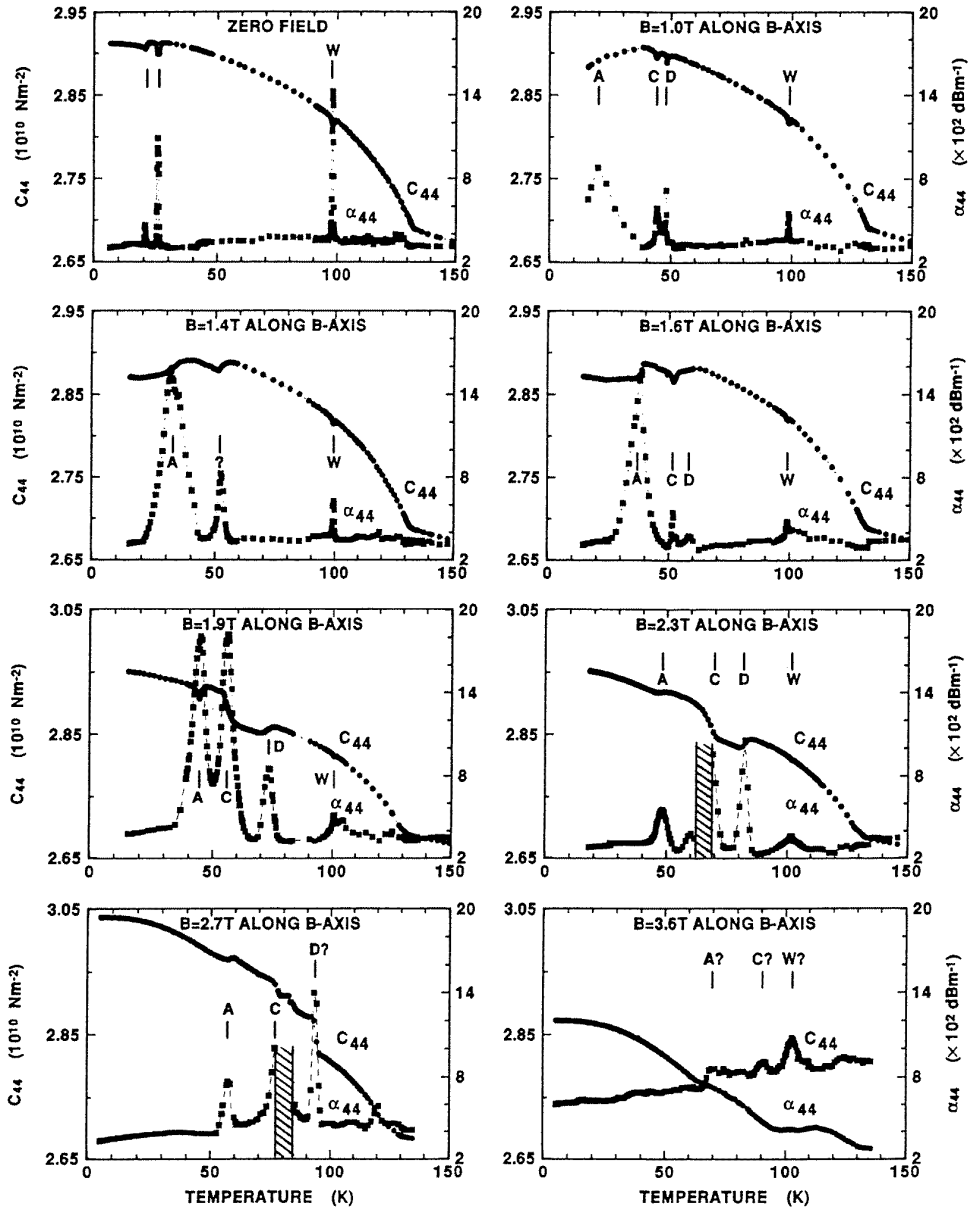

Figure 18. Isofield measurements of the shear elastic constant C_{44} and attenuation coefficient α_{44} measured on crystal Ho2 during increasing temperature runs. Magnetic fields as indicated were directed along the *b* axis. Special features associated with these curves are marked with short vertical lines and denoted with letters A, C, D, and W. Temperatures where these features appear are plotted in figure 19, giving rise to similarly marked branches on our phase diagram.

give results that agree within experimental error with the results found for fields along the *b* axis. For fields applied along the *c* axis the magnitude of the drop in C_{33} and T_N remains unchanged from that observed in zero field and no second step in C_{33} develops. This presumably corroborates the finding by Noakes *et al* [12] that a *c*-axis-directed field

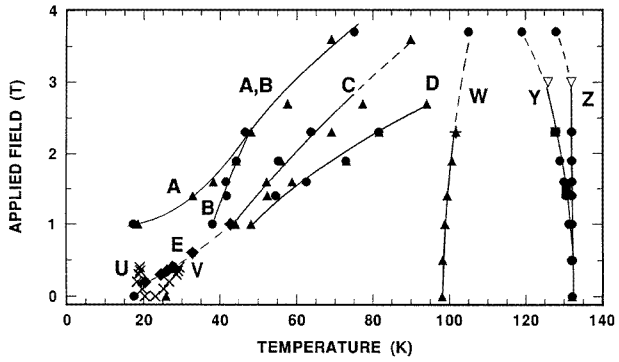

Figure 19. A phase diagram with field directed along the *b* axis of the Ho crystal as deduced from figures 17 (circles) and 18 (triangles) and incorporating parts of phase diagrams given in figures 5 (crosses, lines U and V), 12 (line W), and 16 (lines Y and Z). The significance of the various lines is discussed in the text.

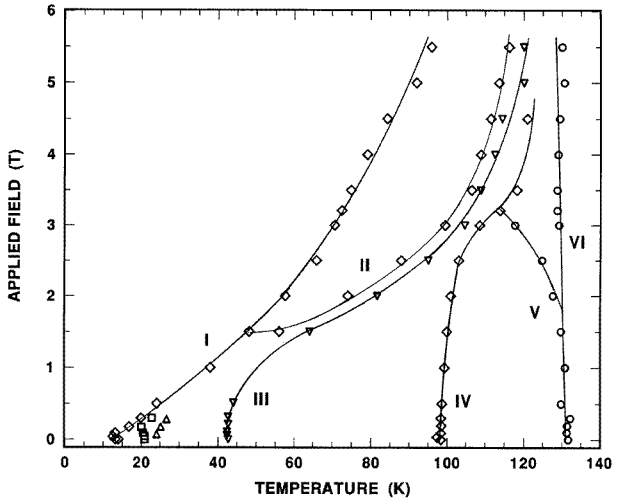

Figure 20. A phase diagram with field directed along the *b* axis of Ho obtained from magnetization measurements by Willis *et al* [42]. A comparison between this diagram and our results in figure 19 is given in the text.

does not lead to lock-in of the wave vector in this temperature region. Finally it is noted that the application of the *c*-axis-directed field shifts the position of the anomaly at T_N to slightly lower temperature.

9. Ultrasonic anomalies in *b*-axis-directed fields

The influence of applied field on the spin-slip structures of Ho is complicated and the tedious process of mapping these structures in the (B, T) plane using neutron diffraction is still in its early stages. Application of macroscopic measurement techniques presents a speedier although indirect way of attempting to construct such phase diagrams. Thus Willis *et al* [42] used the results of bulk magnetization measurements along the principal crystal axes

of Ho in magnetic fields up to 5.5 T in order to construct phase diagrams pertaining to the slip-slip behaviour and the field dependence of the transition temperatures T_C and T_N. Other bulk properties may also be used, and in a study on erbium a.c. susceptibility and electrical resistivity proved to be useful in order to indicate spin-slip temperatures in the zero-field case [43]. Features such as a peak or a maximum in the magnetization curve or inflexion point on this curve are used as criteria for locating the various phase transition points or spin-slip temperatures as is evident from the paper on holmium [42].

As a modest contribution towards establishing (B, T) phase diagrams for spin-slip structures in Ho we consider the temperature dependences of C_{33}, α_{33}, C_{44}, and α_{44} measured on crystal Ho2 in various *b*-axis-directed fields. Some representative isofield results obtained during heating runs are indicated for C_{33} and α_{33} in figure 17 and for C_{44} and α_{44} in figure 18. For isofield curves up to 2.3 T any heating run was preceded with a cooling run (not shown) which started in the paramagnetic region. Isofield curves in higher fields were obtained using a superconducting magnet and in these cases the sample was magnetized at 4 K by increasing the field from zero to its required value, having prior to this allowed the sample to cool in zero field from the paramagnetic region. Non-exponential echo patterns preclude attenuation measurements in some temperature intervals as indicated by hatched regions on the graphs. Prominent features such as steps or inflection points in elastic moduli appearing in conjunction with peaks in the attenuation coefficient are marked in figures 17 and 18. From ultrasonic studies [11] in zero field it is known how the C_{33} and C_{44} modes couple with specific spin slips (see table 1). The anomalies that we clearly observe are those at T_C and T_N and those associated with spin-slip behaviour at 26 and 98 K. We attempt to follow and locate these anomalies in the isofield curves and plot them on a (B, T) diagram in figure 19. This is not always a straightforward matter because of the sometimes rapidly changing nature of the ultrasonic parameters from one isofield value to the next. Hence, the detail of how at low temperature the zero-field C_{44} and α_{44} anomalies transform to the measured results at 1 T has not been followed. It is also seen that the two anomalies indicated with C and D in figure 18 for $B = 1$, 1.6, 1.9, and 2.3 T appear as a single attenuation peak for the $B = 1.4$ T isofield curve. Furthermore it is recognized that the assignments given in figure 17 for $B = 3.7$ T and in figure 18 for $B = 3.6$ T are rather tentative. Some new features appear when a magnetic field is applied and these give more phase lines than one would expect from the zero-field results. We incorporated points from the phase diagrams given in figures 5, 12, and 16 as determined by neutron diffraction and ultrasonics in constructing figure 19. The lines drawn in figure 19 are guides to the eye and are to be compared with the phase diagram for *b*-axis-directed fields given by [42] and reproduced as figure 20.

Comparison of figures 19 and 20 seems to indicate that line I of [42] corresponds to our line labelled A, but we do not find evidence in our work of line II branching off from line I. Our diagram shows some additional structure indicated as line B which joins with line A at 2 T. Line III is not observed in our experiments since the C_{33} and C_{44} modes do not couple with the $\boldsymbol{\tau} = \frac{1}{5}\,\boldsymbol{c}^*$ structure. Consequently the presence of lines C and D on our diagram implies the existence of an extra line in comparison with [42]. The region between lines Y and Z in figure 19 is known to bracket the $\boldsymbol{\tau} = \frac{5}{18}\,\boldsymbol{c}^*$ structure as indicated in a consistent manner by both neutron-scattering and ultrasonic C_{33} measurements. The width of this region at 3 T is 6 K in figure 19, whereas a width of 12 K at 3 T is indicated between lines V and VI in figure 20. This casts doubt on whether lines IV and V should join up as indicated in [42]. Indeed neutron scattering indicates a more complicated spin-slip behaviour in this region [14]. The phase lines U and V in figure 19 bracket a region where $\boldsymbol{\tau} = \frac{2}{11}\,\boldsymbol{c}^*$ is the prevailing spin-slip structure, but as is evident from section 4 the

phase boundaries could not be determined from neutron diffraction for $B \geqslant 0.5$ T. This region seems also to be indicated by Willis *et al* (see figure 20). Finally, we added to figure 19 as line E a set of points (diamonds) which signals the temperature above which the magnetic intensity on the $(0, 0, 2)$ nuclear peak disappears. This line seems to connect to line C, although it is not evident what the physical reason for the apparent correlation may be.

It is clear from the preceding comparison of the phase diagrams of Willis *et al* and ourselves that only moderate agreement of the location of phase boundaries exists. Such differences may originate from the use of different single crystals. It also indicates the need for further investigations using a multiparameter approach, e.g. also a.c. susceptibility, electrical resistivity, and dilatometry measurements. Ideally such results should be compared and reconciled in order to construct phase diagrams that can be used to guide the more time consuming and expensive programme of unravelling the complicated spin structure of Ho using neutron diffraction. However, it should also be realized that theoretical models of how anomalies in the various bulk properties are related to the different spin-slip structures, and to each other, need mostly still to be developed. Thus the reconciliation of phase diagrams obtained using different techniques may be a difficult task. It is also noted that the phase diagrams in figures 19 and 20 are incomplete since both Willis *et al* and ourselves restricted our measurements to isofield curves. Isothermal runs with increasing or decreasing field scans should yield another set of lines which will divide the (B, T) diagram into blocks suggesting regions of similar spin structure, which are to be compared with neutron diffraction results [4, 6, 7].

10. Conclusion

It has been indicated in this study that the combination of elastic neutron diffraction and ultrasonic measurements in applied magnetic fields can make a valuable contribution to the elucidation of some of the complex phase diagrams associated with the various spin-slip structures of Ho. However, it is clear that far more elaborative studies need to be undertaken while employing a variety of techniques in order to establish details of the many complex spin structures of Ho as a function of temperature and field.

Acknowledgments

The support of the Atomic Energy Corporation of South Africa, in providing equipment, running costs, and neutron beam time, is greatly appreciated. Professor E Fawcett is thanked for the loan of the single crystals used in this study.

References

[1] Koehler W C, Cable J W, Wilkinson M K and Wollan E O 1966 *Phys. Rev.* **151** 414
[2] Felcher G P, Lander G H, Arai T, Sinha S K and Spedding F H 1976 *Phys. Rev.* B **13** 3034
[3] Pechan M J and Stassis C 1984 *J. Appl. Phys.* **55** 1900
[4] Koehler W C, Cable J W, Child H R, Wilkinson M K and Wollan E O 1967 *Phys. Rev.* **158** 450
[5] Jensen J and Mackintosh A R 1990 *Phys. Rev. Lett.* **64** 2699
[6] Jehan D A, McMorrow D F, Cowley R A and McIntyre G J 1992 *Europhys. Lett.* **17** 553
[7] Jehan D A, McMorrow D F, Cowley R A and McIntyre G J 1992 *J. Magn. Magn. Mater.* **104–107** 1523
[8] Gibbs D, Moncton D E, D'Amico K L, Bohr J and Grier B H 1985 *Phys. Rev. Lett.* **55** 234
[9] Bohr J, Gibbs D, Moncton D E and D'Amico K L 1986 *Physica* A **140** 349
[10] Cowley R A and Bates S 1988 *J. Phys. C: Solid State Phys.* **21** 4113

[11] Bates S, Patterson C, McIntyre G J, Palmer S B, Mayer A, Cowley R A and Melville R 1988 *J. Phys. C: Solid State Phys.* **21** 4125
[12] Noakes D R, Tindall D A, Steinitz M O and Ali N 1990 *J. Appl. Phys.* **67** 5274
[13] Tindall D A, Steinitz M O and Holden T M 1993 *J. Appl. Phys.* **73** 6543
Tindall D A, Steinitz M O and Holden T M 1993 *Phys. Rev.* B **47** 5463
[14] Tindall D A, Adams C P, Steinitz M O and Holden T M 1994 *J. Appl. Phys.* **75** 6318
[15] Tindall D A, Adams C P, Steinitz M O and Holden T M 1994 *J. Appl. Phys.* **76** 6229
[16] Venter A M and du Plessis P de V 1995 *J. Magn. Magn. Mater.* **140-144** 757
[17] Pearce A, Baruchel J and Palmer S B 1991 *Physica* B **174** 121
[18] Cowley R A, Jehan D A, McMorrow D F and McIntyre G J 1991 *Phys. Rev. Lett.* **66** 1521
[19] Mackintosh A R and Jensen J 1991 *Disorder in Condensed Matter Physics* ed J A Blackman and J Taguena (Oxford: Oxford University Press) pp 213–30
[20] Jensen J and Mackintosh A R 1991 *Rare Earth Magnetism: Structures and Excitations* (Oxford: Oxford University Press)
[21] Plumer M L 1991 *Phys. Rev.* B **44** 12 376
[22] Jensen J 1996 *Phys. Rev.* B **54** 4021
[23] Simpson J A, McMorrow D F, Cowley R A and Jehan D A 1995 *Phys. Rev.* **51** 16 073
[24] Cowley R A and Jensen J 1992 *J. Phys.: Condens. Matter* **4** 9673
[25] Jensen J and Cowley R A 1993 *Europhys. Lett.* **21** 705
[26] Steinitz M O, Tindall D A and Adams C P 1995 *J. Magn. Magn. Mater.* **140–144** 759
[27] Venter A M, du Plessis P de V and Fawcett E 1992 *Physica* **180/181** 290
[28] Simpson A M, Jericho M H and Jain M C 1976 *Can. J. Phys.* **54** 1172
[29] Du Plessis P de V, Venter A M and Brits G H F 1995 *J. Phys.: Condens. Matter* **7** 9863
[30] Venter A M, du Plessis P de V, Eloff G A and Fawcett E 1990 *J. Phys.: Condens. Matter* **2** 1363
[31] Van Doorn C F, van Delden D C and du Plessis P de V 1982 *J. Magn. Magn. Mater.* **27** 124
[32] Palmer S B and Lee E W 1972 *Proc. R. Soc.* A **327** 519
[33] Rosen M, Kalir D and Klimker H 1974 *J. Phys. Chem. Solids* **35** 1333
[34] Tachiki M, Lee M C, Treader R A and Levy M 1974 *Solid State Commun.* **15** 1071
[35] Pearce A, Baruchel J and Kulda J 1992 *Phys. Status Solidi* b **172** 443
[36] Baruchel J, Drillat A, Fort D, Jones D W, Palmer S B and Schlenker M 1983 *J. Magn. Magn. Mater.* **31–34** 183
[37] Drillat A, Baruchel J, Bates S and Palmer S B 1984 *J. Magn. Magn. Mater.* **44** 232
[38] Lee M C, Treader R A and Levy M 1972 *Phys. Lett.* **38A** 399
[39] Lee M C, Treader R A and Levy M 1975 *J. Phys. Chem. Solids* **36** 1281
[40] Simpson A M, Jerico M H and Roger W A 1979 *Can. J. Phys.* **57** 385
[41] Venter A M, du Plessis P de V and Fawcett E 1992 *J. Magn. Magn. Mater.* **104–107** 1517
[42] Willis F, Ali N, Steinitz M O, Kahrizi M and Tindall D A 1990 *J. Appl. Phys.* **67** 5277
[43] Willis F and Ali N 1992 *J. Alloys Compounds* **181** 287